Experimental Assessment of the Accuracy of an Advanced Photonic-Bandgap-Fiber Model

Kiarash Zamani Aghaie, *Student Member, IEEE*, Michel J. F. Digonnet, and Shanhui Fan, *Fellow, IEEE*

***Abstract*—From scanning-electron microscope images of the cross section of a photonic-bandgap fiber (NKT Photonics' HC-1550-02) we developed a realistic model for its permittivity profile that includes all observable structural deformations in the core and in the first two rows of cladding holes. Using this more accurate index profile in our C++ full-vectorial finite-difference mode solver, we numerically studied this fiber's modal dispersion, along with the intensity profile, group index spectrum, and group-velocity dispersion spectrum of its fundamental mode. Comparisons between these predictions and their experimental counterparts measured in the fiber show good quantitative agreement for all these characteristics. On the other hand, when these structural deformations are purposely not included in the permittivity profile, the predicted and measured characteristics generally poorly match. The study demonstrates that first, accurate simultaneous predictions of several key modal characteristics of hollow-core fibers can be obtained numerically, and that although small, the aforementioned index-profile perturbations must be included in order to obtain sufficient accuracy.**

***Index Terms*—Finite-difference methods, hollow-core fibers, numerical analysis, optical fibers, photonic-bandgap fibers, waveguide theory.**

I. INTRODUCTION

HOLLOW-CORE photonic-bandgap fibers (PBFs) have attracted significant attention due to their unique properties [1]. Because in these fibers light is mostly confined in air instead of a solid as in conventional fibers, PBFs exhibit reduced nonlinear and thermal effects, and they have found key applications in fiber optic gyroscopes [2] and other sensors [3]. They also enable transmission at wavelengths where the absorption of usual fiber materials (e.g., glasses) is very high [4].

In order to predict the modal properties of hollow-core fibers, several numerical methods have been developed, based on finite-element methods (FEM) [5], finite-difference methods [6], [7], plane-wave expansion [8], beam-propagation method [9], or multipole method [10]. These methods differ mostly in their speed of convergence and relative accuracy. In all cases, the most critical input parameter is the refractive-index profile of the PBF. An example of such a profile is shown in Fig. 1 for NKT Photonics' HC-1550-02 fiber, currently the most popular commercial 7-cell PBF and the object of this study. Various levels of approximations have been used to model this rather complex two-dimensional index profile. In early studies, it was simply approximated as a perfect periodic structure in which a circular hole had been punched to form the core [6]. Later models refined this approach by approximating the cladding holes by identical hexagons with rounded corners, and the core by a larger dodecagon with rounded corners and a constant wall thickness [11]. Still later developments adjusted the size and shape of the first row of holes surrounding the core to account for the obvious deformations taking place in this region during fiber drawing (see Fig. 1) [12]. For even more faithful representations, scanning-electron microscope (SEM) images of either the core region or the whole fiber cross section were digitized and the resulting profile was numerically simulated [13]–[15].

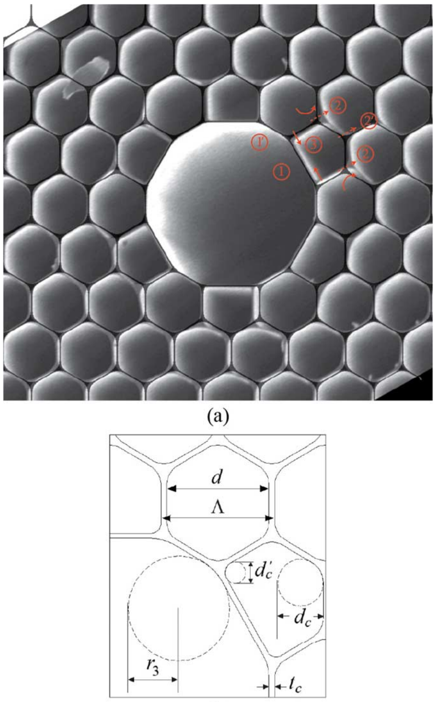

(a)

(b)

Fig. 1. (a) SEM image of the HC-1550-02 fiber. The conventionally used permittivity profile is overlaid on the image. The arrows illustrate the structural distortions on air holes not accounted for in this profile. Perturbations on the first two rows of holes are identified by numbers. (b) Magnified portion of this profile showing the profile parameters.

Interestingly, even though we expect that these increasingly more refined descriptions should predict the properties of these

---

Manuscript received September 30, 2012; revised December 14, 2012; accepted January 03, 2013. Date of publication January 11, 2013; date of current version February 06, 2013. This work was supported by Litton Systems, Inc., a wholly owned subsidiary of Northrop Grumman Corporation.

The authors are with the Edward L. Ginzton Laboratory, Stanford University, Stanford CA 94305 USA (e-mail: kzamani@stanford.edu; silurian@stanford.edu; shanhui@stanford.edu).

Color versions of one or more of the figures in this paper are available online at http://ieeexplore.ieee.org.

Digital Object Identifier 10.1109/JLT.2013.2238608

fibers increasingly more accurately, only a few publications report a quantitative comparison between the predicted and measured properties of a PBF [13]–[17]. Much of these studies were confined to qualitative comparisons between measured loss spectra and calculated modal dispersion diagrams, or between calculated and measured mode intensity profiles [13], [16].

Although it is reasonable to expect that digitizing the SEM image of the fiber core and a few of its surrounding rings of air holes, as done in [13]–[15], should be a faithful method for modeling a PBF's index profile, the accuracy may be limited by the spatial resolution of large SEM images [15]. In this paper, we circumvent this problem by limiting the field of view of the SEM image to the core and the first two rings of holes. By careful analysis of the SEM images of the core region of the PBF, we determine the shape and critical dimensions of the core and of each hole in the two rings of air holes surrounding the core, and we replicate these shapes and dimensions in our index-profile model with suitable geometric parameters. The resulting profile therefore includes an accurate description of the deformations that have the greatest influence on the core modes. This approach is also applicable to other types of fibers such as solid-core photonic-crystal fibers [18]. Our mode solver relies on a full-vectorial finite-difference frequency-domain (FDFD) method [19]. It assumes an index profile with the C_{6v} symmetry in order to take advantage of this symmetry and to drastically reduce the computation time and memory requirement. Some averaging of the measured hole shapes and dimensions is therefore applied to ensure that the input profile retains this idealized C_{6v} symmetry (even though the fiber does not have perfect C_{6v} symmetry). The modal characteristics of the fiber are then computed with the mode solver.

This paper has several main purposes. First, it aimed to incorporate in our existing mode solver the aforementioned advanced model of the fiber index profile obtained from SEM photographs. The second objective was to assess the accuracy of this index-profile model by performing a quantitative comparison of fiber characteristics predicted by the mode solver to their experimental counterparts, measured in the same fiber. This was done for a much larger number of fiber characteristics than previously reported, including the two-dimensional intensity profile, the group index spectrum, and the group velocity dispersion (GVD) spectrum of the fundamental mode, as well as the absolute band edge frequencies. The main goal of this comparison was to determine whether the spatial definition of the index model we propose is high enough to provide an accurate description of a broad range of fiber characteristics. A positive answer to this question would provide evidence that the method used to define the index profile is adequate to model the basic electromagnetic properties of a hollow-core fiber. A negative answer would point to the need to identify more precise methods to define the nanometric features of the internal structure of a typical hollow-core fiber.

As mentioned earlier, this study was conducted with NKT Photonics' HC-1550-02 fiber. Comparison between our code's predictions and the measured characteristics of this fiber's fundamental mode show that numerical simulations utilizing the aforementioned index-profile model give accurate quantitative predictions for all these properties, and significantly more accurate predictions than the earlier index-profile model. We demonstrate in particular good agreement between (1) the predicted dispersion spectrum and the measured loss spectrum (e.g., the difference between the predicted and measured two avoided crossing points is less than 12 nm); (2) the predicted and measured intensity profiles (the difference between $1/e^2$ full widths is only 1.2%); (3) the predicted and measured group index spectrum; and (4) the predicted and measured GVD spectrum over a broad spectral range.

II. NEW REALISTIC PERMITTIVITY MODEL AND ITS PROFILE GENERATION METHOD

We took multiple SEM images of the fiber under study, using different magnifications and focusing on different areas of the cleaved fiber end in order to obtain high resolutions of the various features that most affect the profile of the fundamental mode. These features include the core and its membranes, the first two rows of cladding holes surrounding the core, and the rows of cladding holes far away from the core. We did not sputter gold on the fiber end since such sputtering can introduce an uncertainty on the thickness of the membranes. The SEM image exhibited some charging due to the lack of a conductive path, but the images were sharp enough for our purpose.

Fig. 1(a) shows a general SEM view of the fiber end. As a point of reference, we also display in Fig. 1 the permittivity profile model that we and others used in previous modal analysis of this fiber [11], [20], overlaid in Fig. 1(a) on the SEM photograph. In these earlier studies, the core ring was modeled as a dodecagon with rounded corners, a constant thickness t_c, and a constant radius. This core ring perturbs its neighboring air holes. Six of the holes in the first row were modeled as pentagons. The corners of these pentagons were rounded with two different diameters, d_c and d'_c (Fig. 1(b)). The other holes in the first row and in the PC cladding were modeled as identical hexagons with a width d and corners rounded with a diameter d_c. The pitch of the PC cladding was Λ. In [12], the authors went one step further and introduced a parameter for the core radius.

Although there is general visual agreement between this earlier idealized profile and the SEM image, there are some obvious discrepancies (see Fig. 1(a)). The most prominent one is that the first two rows of holes are significantly perturbed from their nominal shapes. To faithfully model the modal characteristics of this PBF, we need to modify the permittivity-profile model of Fig. 1(b) so as to account for these perturbations. Fig. 2(a) shows the modified permittivity-profile model used in this paper. This profile introduces five corrections. First, we found that the core wall does not have a constant thickness. Where it adjoins the six hexagon-shaped cladding holes (region labeled 1′ in Fig. 2(a)), the wall has a mean thickness of $t_{c1} = 89\ \mathrm{nm}$. Where it adjoins the six pentagon-shaped holes (labeled 1), the mean thickness is $t_{c2} = 151\ \mathrm{nm}$.

Second, the pentagon-shaped holes in the first row are elongated in the radial direction (identified in Fig. 2(a) by the dashed straight arrows labeled 2 and 2′), and they are compressed in the azimuthal direction (solid straight arrows labeled 3). These

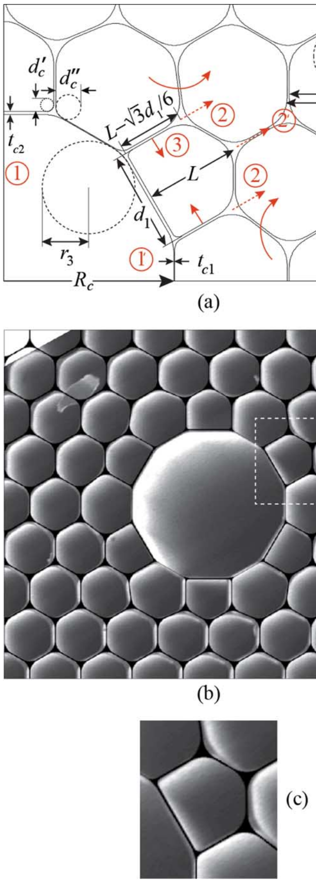

Fig. 2. (a) The parameters of our proposed permittivity-profile model. The arrows depict the structural distortions in the first and second rows of cladding holes. Numbers inscribed in circles identify the major perturbations. (b) Our proposed permittivity-profile model overlaid on top of one of our SEM images. (c) The enlarged view of the region marked by dashed lines in (b).

deformations are taken into account in the new model with parameters L and d_1, respectively (see Fig. 2(a)). Third, the corners of the six hexagon-shaped holes in the first row do not have the same curvature. The two corners against the core are rounded with a new diameter d_c'', whereas the other four corners are rounded by the same diameter d_c (see Fig. 2(a)). The mean measured value of d_c'' (845 nm) is considerably smaller than that of d_c (2.15 μm). Fourth, some membranes at the boundary between the first and second row, identified by curved arrows in Fig. 2(a), are displaced from their nominal locations. Fifth, this perturbation also compresses twelve holes in the second row (holes that contain the dashed arrows labeled as 2). These last two perturbations were already taken care of when applying the second perturbation discussed above. The mean and the standard deviation values of all these parameters are summarized in Table I.

Because parameters Λ, d, and d_c determine the bandgap, they must be estimated from unperturbed holes. For this purpose, we measured these parameters from SEM images of the holes in the third and fourth rows. Their measured mean values are listed in Table I. The thickness of the membranes in the PC cladding, i.e., $\Lambda - d$, is ~110 nm, corresponding to an air-filling ratio of 91.7%. This is consistent with the value cited by NKT Photonics (>90% [21]).

TABLE I
THE MEAN VALUE AND STANDARD DEVIATION OF OUR PROPOSED PERMITTIVITY-PROFILE-MODEL PARAMETRS

Parameter	Mean value	Standard deviation
Λ	3.88 μm	81 nm
d	3.77 μm	84 nm
d_c	2.15 μm	53 nm
R_c	5.82 μm	90 nm
t_{c1}	89 nm	10 nm
t_{c2}	151 nm	7.6 nm
r_3	1.58 μm	43 nm
d_c'	445 nm	32 nm
d_c''	845 nm	61 nm
L	3.38 μm	80 nm

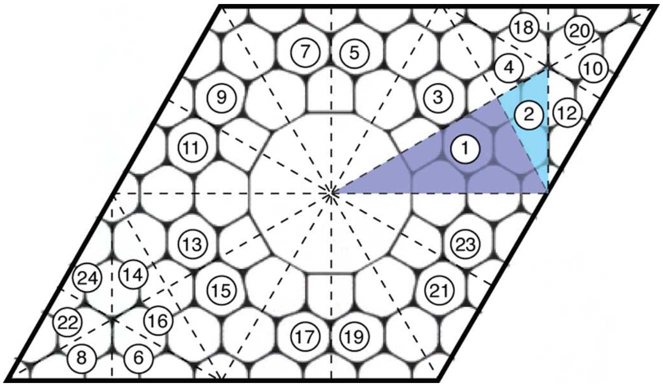

Fig. 3. Lozenge-shaped computational window used in our FDFD method. The shaded triangles represent 1/12th of the total window. Dashed lines show the boundaries of the different regions.

We used our C++ FDFD solver for the modal analysis of the fiber [19]. This method uses a lozenge-shaped computational window, with periodic boundary condition imposed on its boundaries (Fig. 3) [19]. In our previous publications, we generated the permittivity profile in the total window. However, the fiber's C_{6v} symmetry can be used to reduce its description to only 1/12th of the window, which reduces computation time and simplifies the generation of our complicated permittivity profile.

To this end, we developed a new algorithm in which the total computational window is divided into 24 triangular regions, outlined by the dashed lines in Fig. 3. The shaded regions labeled 1 and 2 compose the irreducible 1/12th of the window. We only describe the permittivity profile in these regions. The permittivity at any point outside of these regions is then simply calculated by finding the corresponding point in these shaded regions by a combination of reflections, rotations, and translations permitted by the fiber symmetry. These transformations are summarized in Table II. The identity transformation is represented by I. Reflection with respect to a plane characterized by its orientation angle α, where $\alpha \in \{0, \pi/6, \pi/3, \pi/2, -\pi/6, -\pi/3\}$, and rotation by angle α, where $\alpha \in \{\pi/3, 2\pi/3, \pi, -\pi/3, -2\pi/3\}$, are denoted by σ_α and R_α, respectively. T_1 and T_2 stand for translations along the horizontal direction and at 60° to the horizontal direction, respectively.

The permittivity profile obtained from this replication process using our measured parameter values is shown in Fig. 2(b). An

TABLE II
THE TRANSFORMATION TABLE OF DIFFERENT REGIONS IN OUR COMPUTATIONAL WINDOW

Region number	Corresponding region number	Transformation
1	1	I
2	2	I
3	1	$\sigma_{\pi/6}$
4	2	$\sigma_{\pi/6}$
5	1	$R_{\pi/3}$
6	2	$R_{\pi/3}-T_2$
7	1	$\sigma_{\pi/3}$
8	2	$\sigma_{\pi/3}-T_2$
9	1	$R_{2\pi/3}$
10	2	$R_{2\pi/3}+T_1$
11	1	$\sigma_{\pi/2}$
12	2	$\sigma_{\pi/2}+T_1$
13	1	R_{π}
14	2	R_{π}
15	1	$\sigma_{-\pi/3}$
16	2	$\sigma_{-\pi/3}$
17	1	$R_{-2\pi/3}$
18	2	$R_{-2\pi/3}+T_2$
19	1	$\sigma_{-\pi/6}$
20	2	$\sigma_{-\pi/6}+T_2$
21	1	$R_{-\pi/3}$
22	2	$R_{-\pi/3}-T_1$
23	1	σ_0
24	2	σ_0-T_1

enlarged view of the region marked with the dashed lines is presented in Fig. 2(c). This profile clearly matches the SEM image much more closely than the previous profile (Fig. 1(a)). By modifying the conventionally used permittivity-profile model, we have significantly reduced the mismatch between the numerical index profile and the real profile. The residual mismatch can be attributed to a large extent to the departure of the actual profile from true C_{6v} symmetry.

III. COMPARISON BETWEEN NUMERICAL AND MEASUREMENT RESULTS

We analyzed the fiber of Fig. 1 with the realistic permittivity profile described in the last section and the parameters of Table I. We run the simulations on Stanford University's cluster of 8-core 2.7-GHz AMD Opteron processors. The computational window, shown in Fig. 3, was $8\Lambda \times 8\Lambda$ in size, which enabled us to model the core along with around three rows of holes. The spatial resolution was $\Delta s = 24.25\ \mathrm{nm}$, or equivalently 160 grid points in one period. We used sub-pixel averaging to improve convergence, as described in [19]. To ensure that coupling between fibers in different supercells does not change the predicted results, we also calculated the effective indices of the fiber core modes using a $10\Lambda \times 10\Lambda$ window (around four rows of holes). When using either window, the calculated effective indices did not change appreciably across the bandgap (by less than 0.1% for the fundamental mode and 1.3% for higher order modes). It showed that the $8\ \Lambda \times 8\ \Lambda$ window was adequate for modeling this mode. The calculated modal characteristics presented below were generated using this window size.

A. Modal Dispersion Diagram and Measured Loss Spectrum

The calculated modal dispersion diagrams for the propagating modes are plotted in Fig. 4(a). There are a total of 11 surface modes in the bandgap, four doubly-degenerate (shown as red dashed curves) and three singly-degenerate (dashed-dotted red curves). The doubly-degenerate surface modes that have the same symmetry as the HE_{11} mode interact with this mode at the avoided crossing points $\lambda_C = 1474\ \mathrm{nm}$ and $\lambda_E = 1746\ \mathrm{nm}$ (the doubly-degenerate surface mode that crosses the HE_{11} mode just to the right of λ_E does not have the right symmetry to interact with the HE_{11} mode.) There is another avoided crossing point between the HE_{11} mode and the lower band-edge mode at $\lambda_B = 1426\ \mathrm{nm}$. These avoided crossing points divide the HE_{11} mode dispersion curve into three transmission bands: the first from λ_B to λ_C, the second from λ_C to λ_E, and the third from λ_E to $\lambda_G = 1785\ \mathrm{nm}$ (plain crossing with the upper band-edge mode). The second band is the widest, with a bandwidth of 272 nm.

Since the effective indices of the core modes cannot be easily measured accurately [22], we compared instead the calculated modal dispersion of the HE_{11} mode with this fiber's uncalibrated measured loss spectrum (see Fig. 4(a)). For this measurement, we coupled light from a superluminescence diode to 2 meters of a standard single-mode fiber (SMF) spliced to a long coil ($\sim$18 m) of our PBF. Using an optical spectrum analyzer (OSA), we measured the transmission spectrum of this spliced fiber assembly, and we normalized it to the spectrum measured when the source is connected to the OSA through 2 meters of the same SMF. This method provided the uncalibrated loss of the PBF in the spectral range of 1407–1675 nm.

Coupling to surface or band-edge modes substantially increases the loss at the avoided crossing points λ_B, λ_C, λ_E. Hence, we expect that the edges of the fiber loss spectrum occur in the vicinity of these wavelengths [13]. The measured loss spectrum consists of three peaks: a large one at 1407 nm and two smaller peaks at 1438 nm and 1468 nm. There is clearly a strong correlation between these three peaks and the avoided crossing points in the dispersion diagram. The small peaks in the measured spectrum are in very good agreement with λ_B and λ_C. The difference between these calculated and measured avoided crossing points is only -12 nm and 6 nm. At wavelengths shorter than λ_B, the optical mode is the superposition of the air-guided HE_{11} mode and the lower band-edge strut (cladding) mode and other very lossy cladding modes. Consequently, as the measured spectrum shows, the mode loss in this wavelength range is high.

For comparison, we also calculated the modal dispersion diagram with the earlier permittivity profile of Fig. 1(a) (Fig. 4(b)). This less accurate profile predicted only eight surface modes in the bandgap and only one avoided crossing point at $\lambda'_E = 1724\ \mathrm{nm}$, dividing the HE_{11} dispersion curve into two transmission bands: a wide band from $\lambda'_B = 1425\ \mathrm{nm}$ to λ'_E and a narrow one from λ'_E to $\lambda'_G = 1763\ \mathrm{nm}$. This model therefore fails to predict the peak at 1468 nm in the measured loss

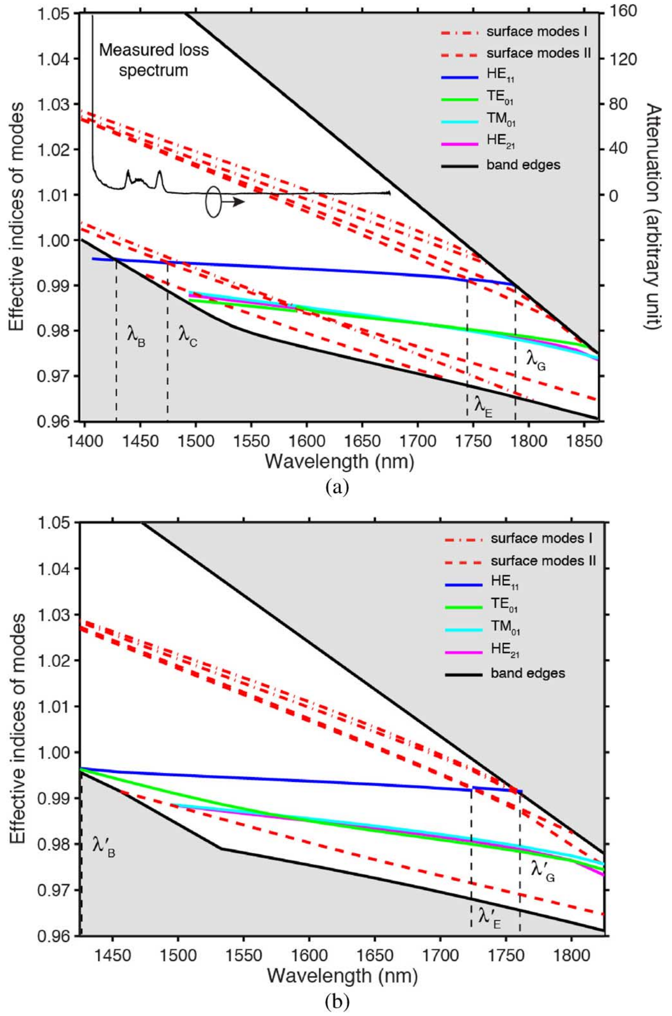

Fig. 4. (a) Modal dispersion diagram of propagating modes, calculated with the model in Fig. 2(a), in our PBF along with the measured uncalibrated propagation loss spectrum. Red dashed and red dashed-dotted curves represent the doubly-degenerate and singly-degenerate surface modes, respectively. (b) Modal dispersion diagram calculated with the model in Fig. 1(b) (color online).

spectrum. This prediction of fewer avoided crossing points is consistent with previous work [16], in which no surface mode was numerically predicted but one was observed in the measured loss spectrum.

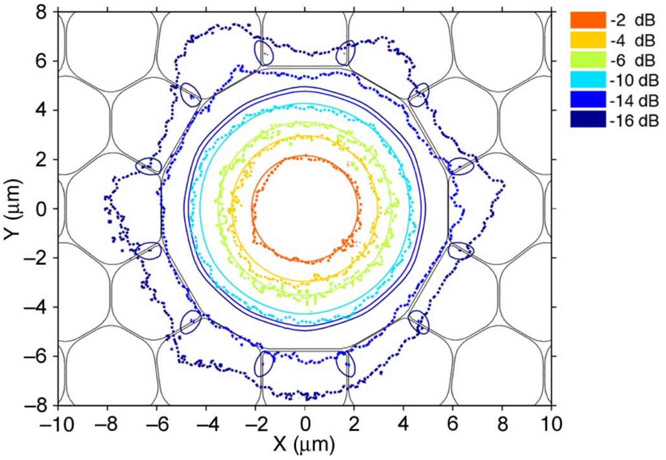

Fig. 5. Logarithmic contour map of the measured intensity profile (dotted curves) superimposed on the calculated intensity profile (solid curves) of the fundamental mode at 1550 nm. The fiber profile is shown in the background (color online).

B. Calculated and Measured Intensity Profiles

The calculated and measured intensity profiles of the HE_{11} mode at 1550 nm are plotted in Fig. 5. For these measurements, light from a 1550-nm laser diode was passed through a polarization controller, then coupled to a long PBF (~18 m). The fiber output was collimated with an aspheric lens and recorded with a Vidicon camera. This imaging system had a calculated optical resolution of $\sim 1.8\ \mu\mathrm{m}$, and the camera pixel size was $\sim 0.03\ \mu\mathrm{m}^2$ (the optical resolution is defined as $0.5\times\lambda/\mathrm{NA}$, where λ is the wavelength (1550 nm) and NA stands for the numerical aperture of our lens). We adjusted the polarization controller to couple equal power into the two HE_{11} eigenpolarizations. The calculated profile in Fig. 5 shows the sum of two eigenpolarizations as well. Both profiles show that there is a very small but noticeable intensity in the core ring and in the first row of air holes (see Fig. 5). There is a good agreement between the calculated and measured profiles for intensities larger than -10 dB. The discrepancy between the profiles for intensities less than -10 dB can be accounted for by the finite resolution of our measurement, as explained further down.

To compare these profiles more fully, we present in Fig. 6 plots of the modal intensities along the x- and y-axis. The mode-field diameter (MFD) of the calculated intensity profile, defined as the $1/e^2$ full width, is 8.05 μm. It agrees well with the measured MFD of 8.15 μm obtained from Fig. 5. To simulate the finite resolution of our measurement, we convolved the predicted x-axis profile of Fig. 6 with Gaussians with different diameters. Convolution with a Gaussian with a $1/e$ diameter of 2.8 $\mu\mathrm{m}$ yielded a profile closely resembling the measured profile (dotted curve in Fig. 6). This indicates that the resolution of the measured profile, at least at low intensities, is most likely close to 2.8 $\mu\mathrm{m}$, which is in reasonable agreement with the calculated resolution of 1.8 $\mu\mathrm{m}$. This discrepancy may be in part due to the lens aberration, which was not taken into account in this calculation. The residual difference at the edges of the mode (around $\pm 10\ \mu\mathrm{m}$) is attributed to the noise floor of the instrument (about -18 dB), which prevented measurement of lower intensities.

C. Predicted and Measured Group Index

To most accurately calculate the group index of the fundamental mode from the HE_{11} mode effective indices, we employed a well-known theory in quantum mechanics called the Feynman-Hellmann theorem [23]. In [19], we showed that Maxwell's equations describing the mode fields in the PBF could be written in the following form

$$\hat{A}|\psi_\beta\rangle = \beta\hat{B}|\psi_\beta\rangle \tag{1}$$

where β is the wave vector along the longitudinal axis, and eigenvector $|\psi_\beta\rangle$ is defined as

$$|\psi_\beta\rangle = \begin{bmatrix}\mathbf{E_T}\\ \mathbf{H_T}\end{bmatrix} \tag{2}$$

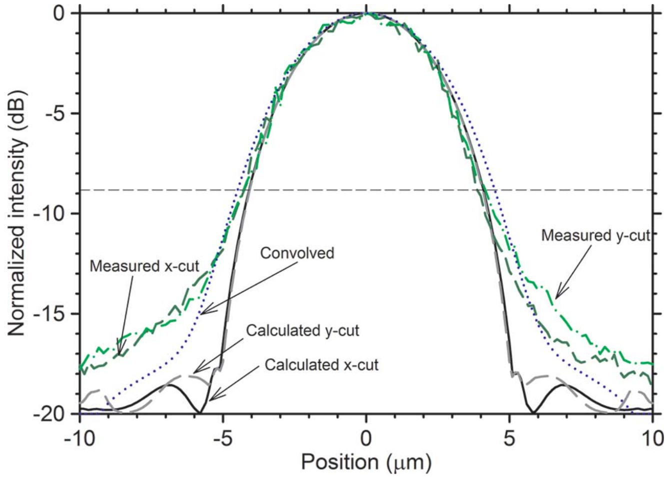

Fig. 6. Line plot of the measured and calculated intensity profile of the HE_{11} mode along the x- and y-axis of Fig. 5. Solid and medium-dashed curves are along the x-axis, and long-dashed and dashed-dotted curves are along the y-axis in Fig. 5. Horizontal dashed line illustrates the $1/e^2$ width (color online).

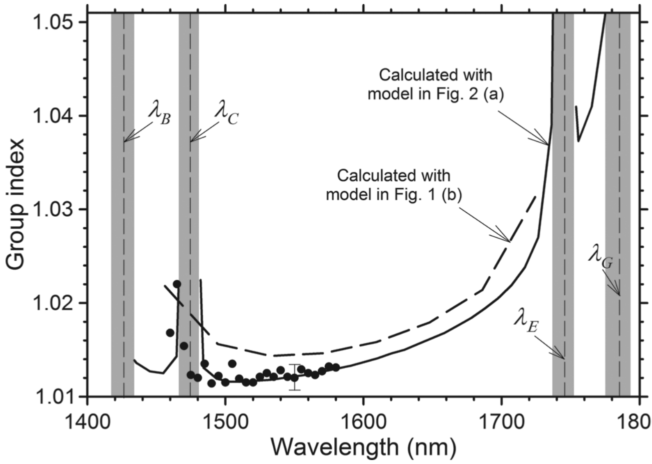

Fig. 7. The calculated group index of the fundamental mode along with the measured group index in the spectral range of 1460–1580 nm (black circles).The vertical dashed lines mark wavelengths in the vicinity of avoided crossing points.

Subscript $\mathbf{T}$ denotes the transverse components of electric and magnetic fields $\mathbf{E}$ and $\mathbf{H}$. Operators $\hat{A}$ and $\hat{B}$ are defined in [19]. The Feynman-Hellman theory states that [23]

$$\frac{d\beta}{d\omega} = \left\langle \psi_\beta \left| \frac{d\hat{A}}{d\omega} \right| \psi_\beta \right\rangle. \tag{3}$$

If we substitute $\hat{A}$ in the above equation, after some simplifications, we obtain

$$\frac{d\beta}{d\omega} = \int dS \left[\overline{\overline{\varepsilon}} |\mathbf{E}|^2 + \mu_o |\mathbf{H}|^2 \right] \tag{4}$$

in which S is the cross section of the PBF, $\overline{\overline{\varepsilon}}$ is the permittivity profile tensor, and $|\mathbf{E}|$ and $|\mathbf{H}|$ denote the magnitude of the total electric and magnetic fields. Since the group index is $n_g = c(d\beta/d\omega)$, we have

$$n_g = \int dS \left[\frac{1}{\eta_o} \overline{\overline{\varepsilon}}_r |\mathbf{E}|^2 + \eta_o |\mathbf{H}|^2 \right] \tag{5}$$

where $\eta_0 = 120\pi$ is the impedance of air and $\overline{\overline{\varepsilon}}_r$ is the relative permittivity profile tensor. The accuracy of the group index calculated with (5) is only limited by the accuracy of the fields, which is significantly higher than the accuracy of the group index directly evaluated from the first derivative with respect to wavelength, which is proportional to $\Delta\lambda$, the separation between the simulated wavelengths.

Fig. 7 shows the calculated group index spectrum (discontinuous solid curves) for the fundamental mode. We have plotted this spectrum only where the mode is mostly confined in air (as occurs in the three surface-mode-free bands in Fig. 4(a)). In the vicinity of λ_B, λ_C, λ_E, and λ_G, the mode is the superposition of the fundamental mode and either a surface mode or cladding modes. In these regions, marked in gray in the figure, the concept of group index is ambiguous, and the group index was not calculated. Due to coupling to surface or cladding modes, the measured group index should exhibit peaks at these wavelengths, as it does. Elsewhere, the group index is very close to unity, as expected. Since the fundamental mode is not well confined in air at wavelengths from λ_E to λ_G [17], the group index is the highest in this band.

To assess the accuracy of these predictions, we measured a portion of the PBF's group index spectrum using a setup similar to the one in Fig. 9 of [24]. Light from a tunable laser (HP Agilent 81682A) was modulated sinusoidally at $f_m = 10\ \mathrm{MHz}$ using an intensity modulator, and coupled into a PBF of length $L \approx 18\ \mathrm{m}$. Using a lock-in amplifier, we recorded the phase of the modulated output signal relative to the phase of the input signal. The group delay through the fiber was obtained from this phase difference $\Delta\phi$ using $\Delta\tau_g = \Delta\phi/2\pi f_m$ [24]. The group index was then calculated from the group delay using $n_g = \Delta\tau_g(c/L)$. The measurement was repeated at multiple wavelengths between 1460 to 1580 nm.

The results are shown as filled circles in Fig. 7. There is excellent agreement between the calculated and measured group indices; their difference falls within our small measurement error (±0.6%, see error bar in Fig. 7). The measured group index reaches a small peak at 1465 nm, in very good agreement with the predicted avoided crossing point at $\lambda_C = 1474\ \mathrm{nm}$. For comparison, in Fig. 7, we have also plotted the group-index spectrum calculated with the more idealistic model shown in Fig. 1(b) (the dashed curve). The group index predicted by this model is higher than the measured spectrum. As expected from the calculated modal dispersion diagram of Fig. 4(b), this model also fails to explain the small peak in the measured group-index spectrum at λ_C.

D. Calculated and Measured GVD

We predict the GVD spectrum of the fundamental mode by direct calculation of the second derivative of the effective indices versus wavelength. The error resulting from this method is proportional to $\Delta\lambda^2$ (The second-order form of the Feynman-Hellmann theory could be used instead; however, it requires the derivatives of fields, which are difficult to calculate, and it does not yield superior accuracy). The solid curve in Fig. 8 shows the

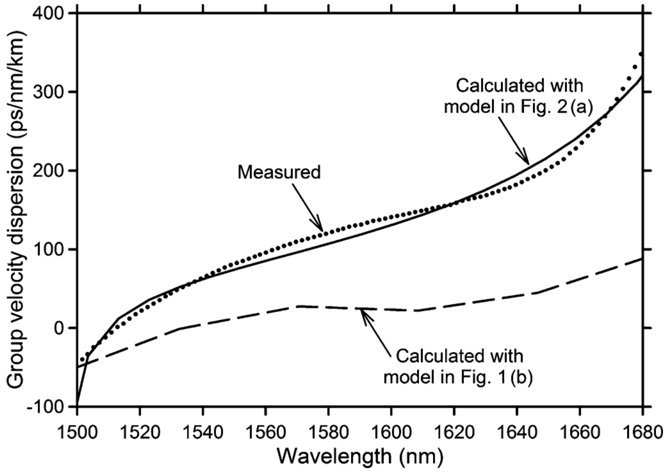

Fig. 8. Measured and calculated GVD spectra of the fundamental mode of the HC-1550-02 fiber.

calculated GVD spectrum. The dotted curve is the GVD spectrum measured by the fiber manufacturer [21]. There is very good agreement between the two spectra over the entire spectral range of the measurement. The difference between the calculated and measured zero-dispersion wavelengths is only -2 nm. To the best of our knowledge, this is the first time that a close agreement between the predicted and measured GVD of a hollow-core fiber over a broad spectral range is reported.

To investigate how much more accurate the predictions made with the advanced index-profile model are, we also calculated the GVD spectrum using the earlier index profile model of Fig. 1(b). The result is plotted as the dashed curve in Fig. 8. This second prediction is obviously in strong disagreement with the measured GVD spectrum. This comparison confirms that the geometrical perturbations introduced in the advanced index-profile model are necessary to predict the GVD spectrum of this fiber accurately.

IV. CONCLUSIONS

We developed a realistic permittivity-profile model of NKT-Photonics' HC-1550-02 fiber that very closely resembles SEM images of the PBF index profile, including distortions of the core thickness and of the first two rows of cladding holes. Using this profile and a C++ full-vectorial finite-difference mode solver, we numerically calculated the fiber's modal dispersion diagram, and the intensity profiles, group index, and group-velocity dispersion of the fundamental mode. To validate this model, we presented a detailed quantitative comparison between these predicted characteristics and their experimental counterparts measured on this fiber. We found that over the bandgap, the fundamental mode couples to the lower band-edge mode at 1426 nm and two doubly-degenerate surface modes at 1474 nm and 1746 nm. These regions of predicted high loss are in good agreement with loss spikes in the fiber's measured loss spectrum. Good agreement was also demonstrated between the calculated and measured intensity profiles of the fundamental mode for both eigenpolarizations, of the group index spectrum, and of the GVD spectrum. When the same fiber was modeled with the more idealized permittivity-profile model used by us and others in the past, we found instead significant disagreement between predictions and experimental data, in particular (1) the avoided crossing point at 1468 nm is missing, which suggests an erroneously wide transmission bandwidth of 299 nm, and (2) the GVD spectrum is significantly off. To the best of our knowledge, this is the first time that a comprehensive quantitative comparison between the calculated and measured characteristics of the modes of a PBF is reported. This study shows that although the deformations in the first two rows of cladding holes are small, it is important to include them in the index-profile model in order to obtain accurate quantitative predictions of these modal characteristics. The next refinement in the accuracy of these predictions will likely be removing the C_{6v} symmetry assumption from the index profile, which will come at the cost of significantly increased computational time.

ACKNOWLEDGMENT

We would like to thank Dr. Jens Lyngsø at NKT Photonics for providing us with their measurement results on their fiber, and Prof. Joseph Kahn for lending us his equipment for measuring the fiber mode's near-field intensity profile.

REFERENCES

[1] F. Benabid, "Hollow-core photonic bandgap fibre: New light guidance for new science and technology," *Phil. Trans. R. Soc. A*, vol. 364, pp. 3439–3462, 2006.

[2] S. Blin, H. K. Kim, M. J. F. Digonnet, and G. S. Kino, "Reduced thermal sensitivity of a fiber-optic gyroscope using an air-core photonic-bandgap fiber," *J. Lightw. Technol.*, vol. 25, no. 3, pp. 861–865, March 2007.

[3] T. Ritari, J. Tuominen, H. Ludvigsen, J. Petersen, T. Sørensesn, T. Hansesn, and H. Simonsesn, "Gas sensing using air-guiding photonic bandgap fibers," *Opt. Exp.*, vol. 12, no. 17, pp. 4080–4087, Aug. 2004.

[4] T. J. Stephens, R. R. Maier, J. S. Barton, and J. D. C. Jones, "Fused silica hollow-core photonic crystal fibre for mid-infrared transmission," presented at the Conference on Lasers and Electro-Optics (CLEO), Postconference Digest, San Francisco, CA, USA, May 2004, Paper CPDD4.

[5] M. Koshiba and K. Saitoh, "Numerical verification of degeneracy in hexagonal photonic crystal fibers," *IEEE Photon. Technol. Lett.*, vol. 13, no. 12, pp. 1313–1315, Dec. 2001.

[6] V. Dangui, M. J. F. Digonnet, and G. S. Kino, "A fast and accurate numerical tool to model the modal properties of photonic-bandgap fibers," *Opt. Exp.*, vol. 14, pp. 2979–2993, April 2006.

[7] Z. Zhu and T. G. Brown, "Full-vectorial finite-difference analysis of microstructured optical fibers," *Opt. Exp.*, vol. 10, no. 17, pp. 853–864, Aug. 2002.

[8] W. Zhi, R. Guobin, L. Shuqin, and J. Shuishen, "Supercell lattice method for photonic crystal fibers," *Opt. Exp.*, vol. 11, no. 9, pp. 980–991, May 2003.

[9] M. Koshiba and K. Saitoh, "Full-vectorial imaginary-distance beam propagation method based on a finite element scheme: Application to photonic crystal fibers," *J. Quantum Electron.*, vol. 38, no. 7, pp. 927–933, Jul. 2002.

[10] T. P. White, R. McPhedran, L. Botten, G. Smith, and C. M. de Sterke, "Calculations of air-guided modes in photonic crystal fibers using the multipole method," *Opt. Exp.*, vol. 9, no. 13, pp. 721–732, Dec. 2001.

[11] F. Poletti, N. G. R. Broderick, D. J. Richardson, and T. M. Monro, "The effect of core asymmetries on the polarization properties of hollow core photonic bandgap fibers," *Opt. Exp.*, vol. 13, no. 22, pp. 9115–9124, Oct. 2005.

[12] R. Amezcua-Correa, N. G. R. Broderick, M. N. Petrovich, F. Poletti, and D. J. Richardson, "Optimizing the usable bandwidth and loss through core design in realistic hollow-core photonic bandgap fibers," *Opt. Exp.*, vol. 14, no. 17, pp. 7974–7985, Aug. 2006.

[13] C. M. Smith, N. Venkataraman, M. T. Gallagher, D. Müller, J. A. West, N. F. Borrelli, D. C. Allan, and K. W. Koch, "Low-loss hollow-core silica/air photonic bandgap fibre," *Nature*, vol. 424, no. 8, pp. 657–659, Aug. 2003.

[14] J. A. West, C. M. Smith, N. F. Borrelli, D. C. Allan, and K. W. Koch, "Surface modes in air-core photonic band-gap fibers," *Opt. Exp.*, vol. 12, no. 8, pp. 1485–1496, Apr. 2004.

[15] M. J. Li, J. A. West, and K. W. Koch, "Modeling effects of structural distortions on air-core photonic bandgap fibers," *J. Lightw. Technol.*, vol. 25, no. 9, pp. 2463–2468, Sep. 2007.

[16] M. N. Petrovich, F. Poletti, A. van Brakel, and D. J. Richardson, "Robustly single mode hollow core photonic bandgap fiber," *Opt. Exp.*, vol. 16, no. 6, pp. 4337–4346, March 2008.

[17] K. Saitoh, N. A. Mortensen, and M. Koshiba, "Air-core photonic band-gap fibers: The impact of surface modes," *Opt. Exp.*, vol. 12, no. 3, pp. 394–400, Feb. 2004.

[18] T. A. Birks, G. J. Pearce, and D. M. Bird, "Approximate band structure calculation for photonic bandgap fibers," *Opt. Exp.*, vol. 14, no. 20, pp. 9483–9490, Sept. 2006.

[19] K. Zamani Aghaie, S. Fan, and M. J. F. Digonnet, "Birefringence analysis of photonic-bandgap fibers using the hexagonal Yee's cell," *IEEE J. Quantum Electron.*, vol. 46, no. 6, pp. 920–930, Jun. 2010.

[20] K. Zamani Aghaie, M. J. F. Digonnet, and S. Fan, "Optimization of the splice loss between photonic-bandgap fibers and conventional single-mode fibers," *Opt. Lett.*, vol. 35, no. 12, pp. 1938–1940, June 2010.

[21] NKT Photonics' HC-1550-02 Datasheet [Online]. Available: http://www.nktphotonics.com/files/files/HC-1550-02.pdf

[22] F. Couny, H. Sabert, P. J. Roberts, D. P. Williams, A. Tomlinson, B. J. Mangan, L. Farr, J. C. Knight, T. A. Birks, and P. St. J. Russell, "Visualizing the photonic band gap in hollow core photonic crystal fibers," *Opt. Exp.*, vol. 13, no. 2, pp. 558–563, Jan. 2005.

[23] R. P. Feynman, "Forces in molecules," *Phys. Rev.*, vol. 56, no. 4, pp. 340–343, Aug. 1939.

[24] H. Wen, M. Terrel, S. Fan, and M. J. F. Digonnet, "Sensing with slow light in fiber Bragg gratings," *IEEE Sensors J.*, vol. 12, no. 1, pp. 156–163, Jan. 2012.

Kiarash Zamani Aghaie (S'05) received the B.S. and M.S. degrees in electrical engineering from the University of Tehran, Tehran, Iran, in 2002 and 2005, respectively. He is currently working toward the Ph.D. degree in electrical engineering of Stanford University, Stanford, CA, USA.

His research interests include computational electromagnetics, and numerical modeling of photonic-bandgap fibers, photonic-crystal fibers, and photonic-bandgap fiber components.

Michel J. F. Digonnet received the degree of engineering from Ecole Supérieure de Physique et de Chimie de la Ville de Paris, the Diplome d'Etudes Approfondies in coherent optics from the University of Paris, Orsay, France, in 1978, the M.S. degree in 1980, and the Ph.D. degree in 1983 from the Department of Applied Physics at Stanford University, Stanford, CA, USA.

His doctoral research centered on WDM fiber couplers and single-crystal fiber lasers and amplifiers. He is a Research Professor in the Department of Applied Physics at Stanford University. His current interests include photonic-bandgap fibers and devices, slow and fast light in fibers, fiber optic gyroscopes, and fiber-based MEMS hydrophones and microphones. He has published about 250 articles, issued over 100 US patents, edited several scientific books, taught courses in fiber amplifiers, lasers, and sensors, and chaired numerous conferences on various aspects of photonics.

Shanhui Fan (M'05–SM'06–F'11) received the Ph.D. degree in 1997 in theoretical condensed matter physics from the Massachusetts Institute of Technology (MIT), Cambridge, MA, USA.

He is currently a Professor of electrical engineering at the Stanford University, Stanford, CA, USA. He was a research scientist at the Research Laboratory of Electronics at MIT prior to his appointment at Stanford. His research interests are in computational and theoretical studies of solid state and photonic structures and devices, especially photonic crystals, plasmonics, and meta-materials. He has published over 260 refereed journal articles that were cited over 16,000 times, has given over 210 invited talks, and was granted 44 US patents.

Prof. Fan received a National Science Foundation Career Award (2002), a David and Lucile Packard Fellowship in Science and Engineering (2003), the National Academy of Sciences Award for Initiative in Research (2007), and the Adolph Lomb Medal from the Optical Society of America (2007). He is a Fellow of the IEEE, the American Physical Society, the Optical Society of America, and the SPIE.